Supporting Information for

A Mechanically Robust Transparent Coating for Anti-icing and Self-cleaning Applications

Xinghua Wu, Zhong Chen*

correspondence to: aszchen@ntu.edu.sg

This PDF file includes:

Supporting information

Figure S1 to S9

Table S1 to S3

Captions for Supporting Videos S1 to S4

Other Supplementary Materials for this manuscript include the following:

Videos S1 to S4

Supporting information

Surface topology of coatings with different sol stirring time

Figure S1 shows AFM images of our coatings with different stirring time (A) 1 day, (B) 4 days, (C) 6 days, (D) 8 days, (E) 10 days and (F) 12 days. Surface roughness of the coatings changes dramatically due to the mechanical dispersion of nanoparticles. The corresponding FESEM images of coatings with different stirring times are shown in Fig. S2. After the 1 day's stirring, the coating surface presented large agglomerated nanoparticles with micro-scale cavities. The continuous application of shear stress drove the nanoparticles to flow and align in certain direction. This process accelerated the detachment of agglomerated nanoparticles, and led to a decreased agglomeration size or even complete elimination of agglomeration of nanoparticles in the coatings. After 12 days' stirring, a very flat and smooth surface with surface roughness around 14.0 nm was obtained. Both the AFM and FESEM images verified the surface morphology and surface roughness change with increasing stirring time of the precursors.

Optical transmittance of coatings

Figure S3 shows the transmittance of the coatings without adding PFOTES with different stirring times. Continuously increasing the stirring time of the precursor sol increased the transmittance of the coatings without PFOTES. At the end of stirring, the coating coated glass approached a stable transmittance of around 80 %, which is lower than that of the transparent coating with PFOTES (~90%).

Due to partial reflections between the interface and various surfaces, precise calculation of two-layer transmittance is complicated and transfer matrix is needed for the

modelling. To simplify the calculation, a first approximation is assumed. The resultant transmittance T of the coated glass slide is given by

$$T = T_g \cdot T_c ,$$ (1)

where T, T_g and T_c are transmittance of glass with the applied coating, the glass slide and the applied coating, respectively. The transmittance index at wavelength of 550 nm was chosen for this calculation. Table S1 shows the calculated transmittance of coatings (with and without PFOTES) with different stirring times at the wavelength of 550 nm. It can be seen that the highest transmittance of coatings without PFOTES was around 89.3%, which is lower than the transparent coatings with PFOTES (97.8%).

Mechanisms of detachment of agglomerated nanoparticles

Assume a shear stress τ is acting on the agglomerated nanoparticles, which is related to the shear rate γ and viscosity μ for Newtonian fluids:

$$\tau = \gamma \mu ,$$ (2)

where μ is a constant. According to a previous report [1], for turbulent flows

$$\gamma = C \cdot \omega^{3/2} ,$$ (3)

where ω is defined as agitation speed which equals to $\left(\frac{2\pi}{60} N \right)$, and N is set as 500 rpm in our experiment and thus, the shear stress can be expressed as

$$\tau = C_1 \cdot \omega^{3/2} ,$$ (4)

where $C_1 = \mu C$.

For large agglomerated nanoparticles, the shear stress-affected area A is large, thus, they are driven by a relative large force F in the solution. The applied driving force not

3

only supports rotation of agglomerated nanoparticles, but also provides a direct external counter force against the van der Waals force and steric hindrance between agglomerated SiO$_2$ nanoparticles.[2, 3] The unbalanced force acting on single nanoparticle will push them moving towards various directions at different speeds; and thus the dispersion status of nanoparticles will be statistically different from each other, leading to detachment of agglomerated nanoparticles as illustrated in Fig. S4. Before the detached SiO$_2$ nanoparticles approach the thermodynamic stability, PFOTES-SiO$_2$ nanoparticles will serve as spacers and graft to the hydrophilic SiO$_2$ nanoparticles by Si-OH groups. Therefore, besides shear stress, the low surface energy PFOTES also plays an important role in the dispersion of nanoparticles. It can graft on nanoparticles in the sol solutions, keeping the nanoparticles from agglomeration by introducing electronegativity and resistance to the van der waals forces.[3-5] The viscosity of the sol solution could be another factor which can withstand the segregation of nanoparticles due to sedimentation.[6] At the end of stirring, all the nanoparticles were uniformly distributed in the sol solution.

Surface chemical structure of the THRC

FTIR spectra of the THRC is shown in Fig. S5. The absorption peak at ~470 cm^{-1} is attributed to the Si-O-Si bond.[7] The absorption peaks between 700 cm^{-1} to 800 cm^{-1} and 1095 cm^{-1} are related to the combined Si-O and Si–C–O stretching groups.[7, 8] Epoxy group are found at ~915 cm^{-1}.[9, 10] The -CF$_3$ and -CF$_2$ groups from PFOTES can be found at 1203 cm^{-1} and 1430 cm^{-1} due to the stretching of C-F bond.[11, 12] The absorption peak at 1739 cm^{-1} is attributed to the stretching of C-O bond.[13] The absorption peaks at 2879 cm^{-1} and

2940 cm^{-1} are assigned to the -CH$_3$ groups.[7] The absorption peak at 1641 cm^{-1} is attributed to the –OH bending due to the absorbed water.[14]

Liquid advancing and receding on the THRC

Figure S6 shows the measured receding and advancing angles of liquids (surface energy ranging from 72.8 to 22.1 mJ/m^2) on the THRC. Generally, the advancing and receding angles decreased with deceasing surface energy of liquids, the unexpected low receding angle of sunflower oil might be due to its fatty acids which have increased the intermolecular interaction with the THRC surface.

Ice adhesion of the transparent coating without PFOTES

Figure S7a compares the ice-adhesion strengths of the uncoated glass, the transparent coating without PFOTES, and THRC coated glass. The surface roughness of all the three coatings fell in the range of 7~33 nm (Fig. S7b and Fig.1). However, due to the hydrophilic properties of uncoated glass (Fig. S7b, with the water contact angle of around 20°) and the transparent coating without PFOTES (Fig. S7b, with the water contact angle of around 60°), these two coatings displayed more than three-times higher ice adhesion than the THRC. Moreover, although the coatings without PFOTES demonstrated great difference in transmittance and surface roughness as stirring time increase, they presented similar water contact angles of 60°~80° (Fig. S7b) with a 10 µl water droplet pinning on their surface. Therefore, less attention was paid on these coatings.

Statistical analysis of icing- temperature of coated and uncoated glass substrates

The measured icing temperature of the THRC coated and uncoated glass is shown in Fig. S8a. The icing temperature represents the beginning of heterogeneous ice nucleation. To comprehensively study the ice nucleation behaviors, 500 cycles of icing and deicing were tested for each sample. Both samples displayed slight increase in the icing temperatures after 300 cycles. This is probably due to a slight spreading of the droplets on surfaces caused by water condensation, which has resulted in a lower water contact angle and a larger water-solid contact area.[15] The THRC sample was less severe in the spreading, which is consistent with the less severe frost formation presented in Fig. 4. The icing temperatures were analyzed by the Gauss normalized distribution curve shown in Fig. S8b, c. The whole icing temperature range was binned with a bin width of 0.2 °C. The Gauss peak temperatures for the maximum freezing events for each sample are shown in Table S2. In addition, the number of freezing events is converted to freezing probability, which is defined as

$$P = \frac{N_i}{N_0} \tag{5}$$

where N_i is the freezing event in the i_{th} bin and N_0 the total icing events (500 in the current study). The survival curve was employed to analyze the distribution. The temperature-survival curve $F(t)$ is defined as [16]

$$F(t) = \frac{N(t)}{N_0} \tag{6}$$

where $N(t)$ is the unfrozen events at temperature t. The obtained results are shown in Fig. S8d. In some reports, the temperature $t_{0.5}$, at which $F(t) = 0.5$, was used as the icing temperature.[17-20] The results are also shown in Table S2 for comparison. A perfect

agreement between the Gauss peak values and $t_{0.5}$ was observed. The mean icing temperature of the THRC glass was ~5°C lower than the uncoated glass substrate.

Furthermore, the icing temperatures have been studied statistically to calculate the nucleation rate of the THRC coated and uncoated samples. According to our previous report [15], the nucleation rate $R(T_i)$ at T_i was binned with a width of ΔT_i which contains n_i freezing events, then

$$R(T_i) = \frac{cn_i}{\Delta T_i \left(\frac{n_i}{2} + \sum_{j>i} n_j \right)}$$

(7)

where c is the cooling rate (5 °C/min in the current experiment), $\sum_{j>i} n_j$ is the sum of unfrozen icing events. Since ice-nucleation site at three-phase contact line was observed directly (Video S3), the corresponding line nucleation rate can be expressed as

$$R_S{}^*(T_i) = \frac{R(T_i)}{S}$$

(8)

where S is the three-phase contact line length between the water droplet and coating surface. It can be calculated by $S = 2\pi r$, where [21]

$$r = \left[\frac{3V}{\pi(2 - 3\cos\theta + cos^3\theta)} \right]^{1/3} \sin\theta$$

(9)

where V is the volume of the water droplet, θ is the Young's contact angle. Since the surface roughness of THRC is less than 15 nm, the measured contact angle can be directly used as θ, and the corresponding S value is listed in Table S3. Accordingly, the calculated $R_S{}^*(T_i)$ of these coatings are shown in Fig. 4c. It can be seen that the ice nucleation rate on the THRC is significantly lower than that on the uncoated glass at the same temperature.
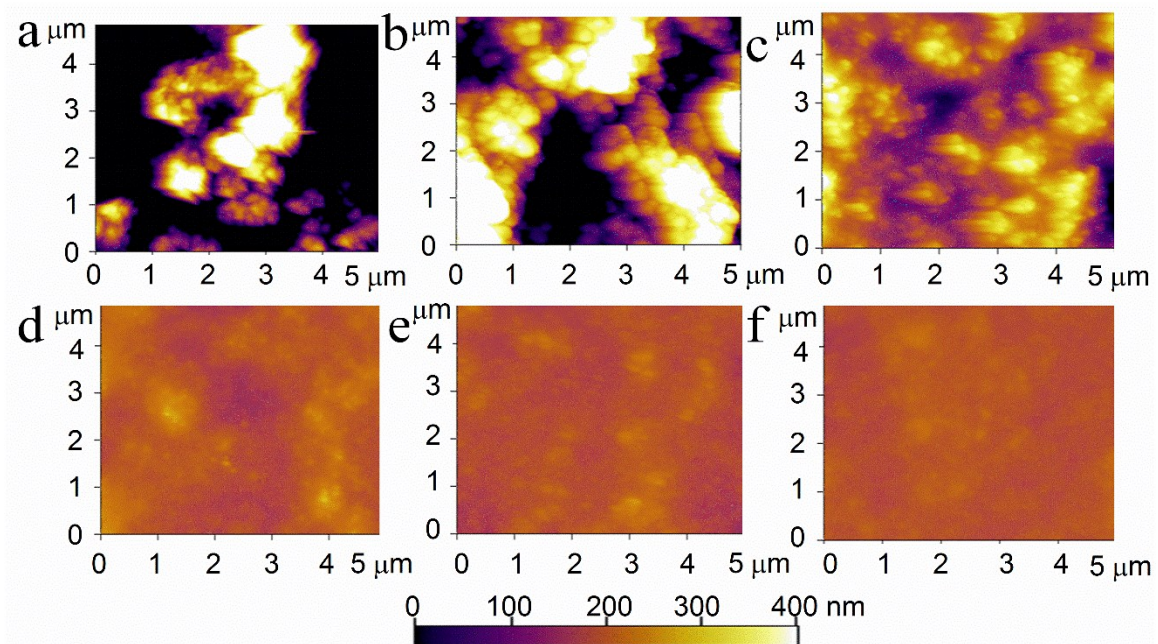
7

Fig. S1. AFM images of our coatings with different stirring time (a) 1 day (305.1 ± 12.7 nm), (b) 4 days (235.0 ± 8.2 nm), (c) 6 days (174.2 ± 6.8 nm), (d) 8 days (43.8 ± 5.0 nm), (e) 10 days (22.4 ± 3.6 nm), (f) 12 days (14.0 ± 1.2 nm). The scale bar of the AFM images is 400 nm.
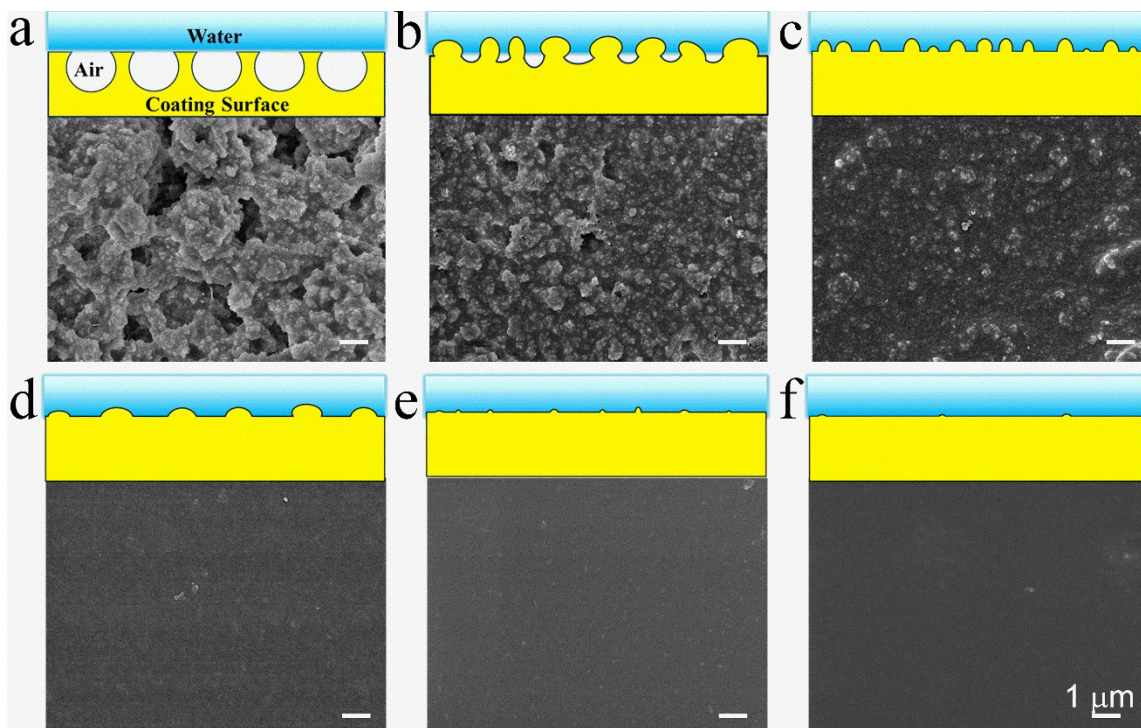
Fig. S2. FESEM images of the coatings with different stirring times of (a) 1 day, (b) 4 days, (c) 6 days, (d) 8 days, (e) 10 days, and (f) 12 days. Insets are schematic illustration of water / coating interfaces.
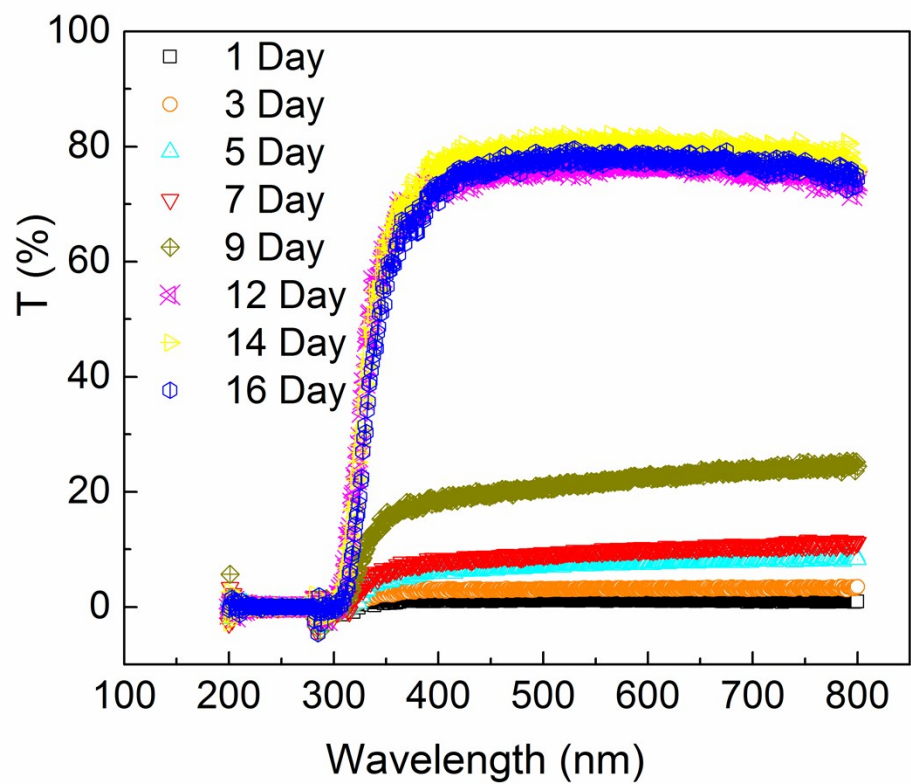
Fig. S3. Transmittance of the coatings without PFOTES after different stirring times.

Table S1. Calculated transmittance of the coatings with different stirring times at the wavelength of 550 nm.

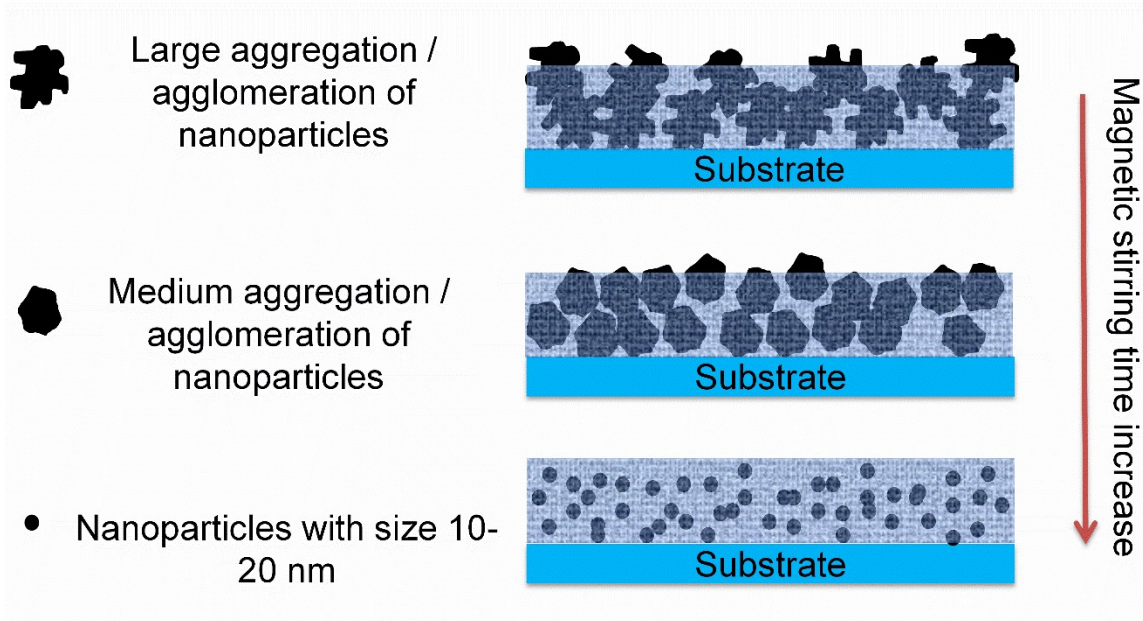| Samples		T	T_g	T_c
PFOTES-coatings	1 day	1.2%		1.3%
	4 days	6.1%		6.7%
	6 days	29.2%	91.4%	32.0%
	8 days	79.9%		87.4%
	10 days	84.7%		92.7%
	12 days	89.4%		97.8%
Coatings without PFOTES	1 day	1.1%		1.2%
	3 days	3.1%		3.4%
	5 days	7.5%		8.2%
	7 days	9.6%		10.5%
	9 days	21.7%	91.4%	23.7%
	12 days	76.6%		83.8%
	14 days	81.6%		89.3%
	16 days	77.8%		85.1%

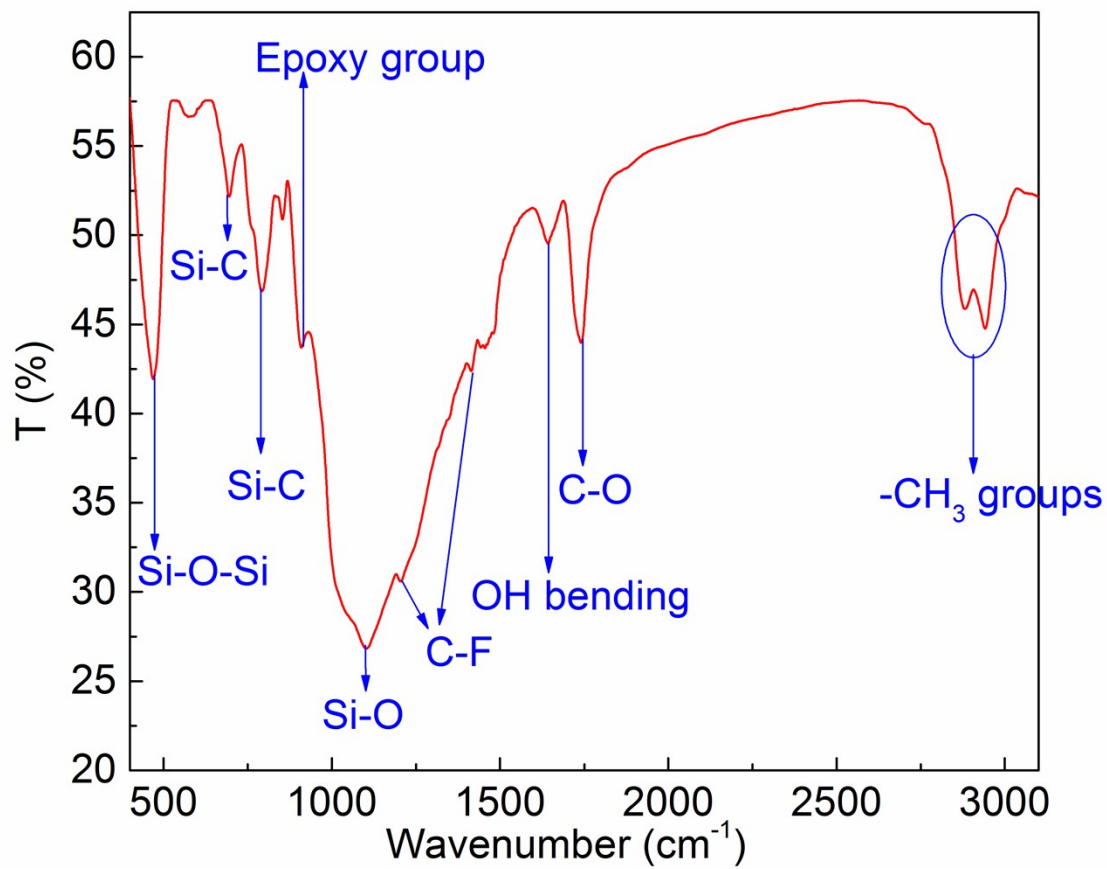Fig. S4. Schematic illustration of detachment of agglomerated SiO_2 nanoparticles.

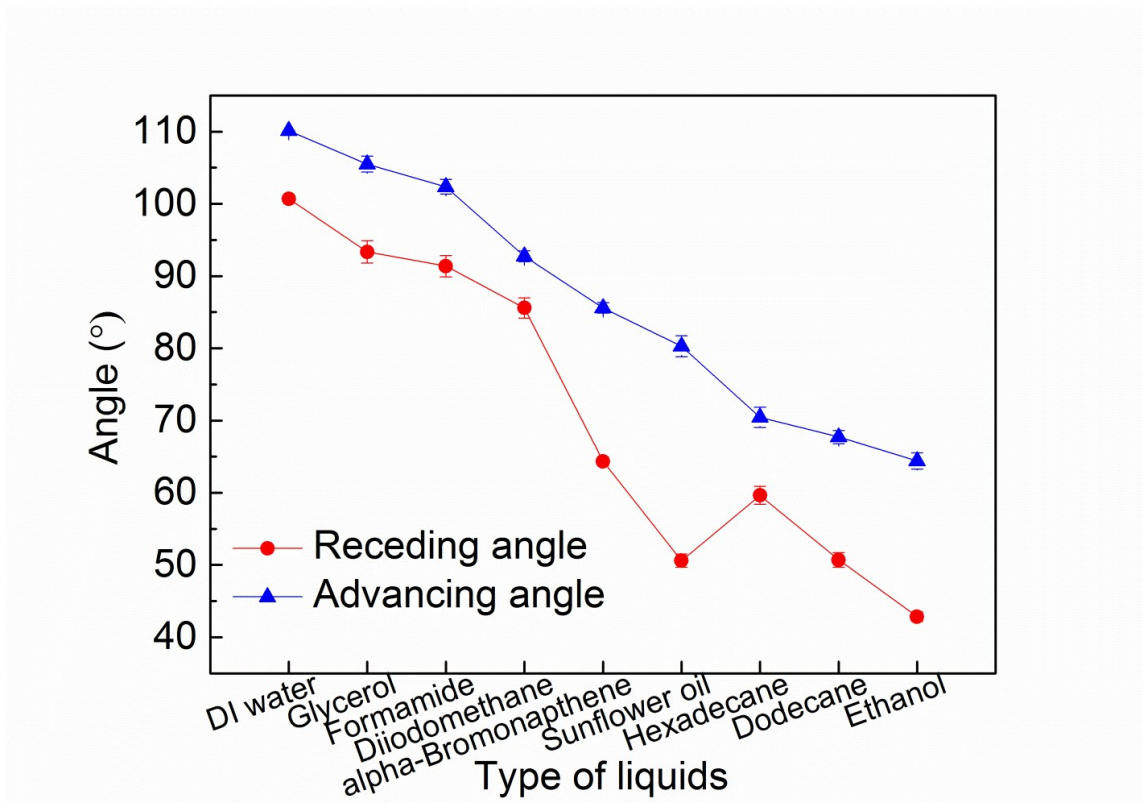Fig. S5 FTIR spectra of the THRC mixed in KBr tablets with weight ratio of 1:20.

Fig. S6. Receding and advancing angles of liquids with surface energy ranging from 72.8 to 22.1 mJ/m^2 on THRC.
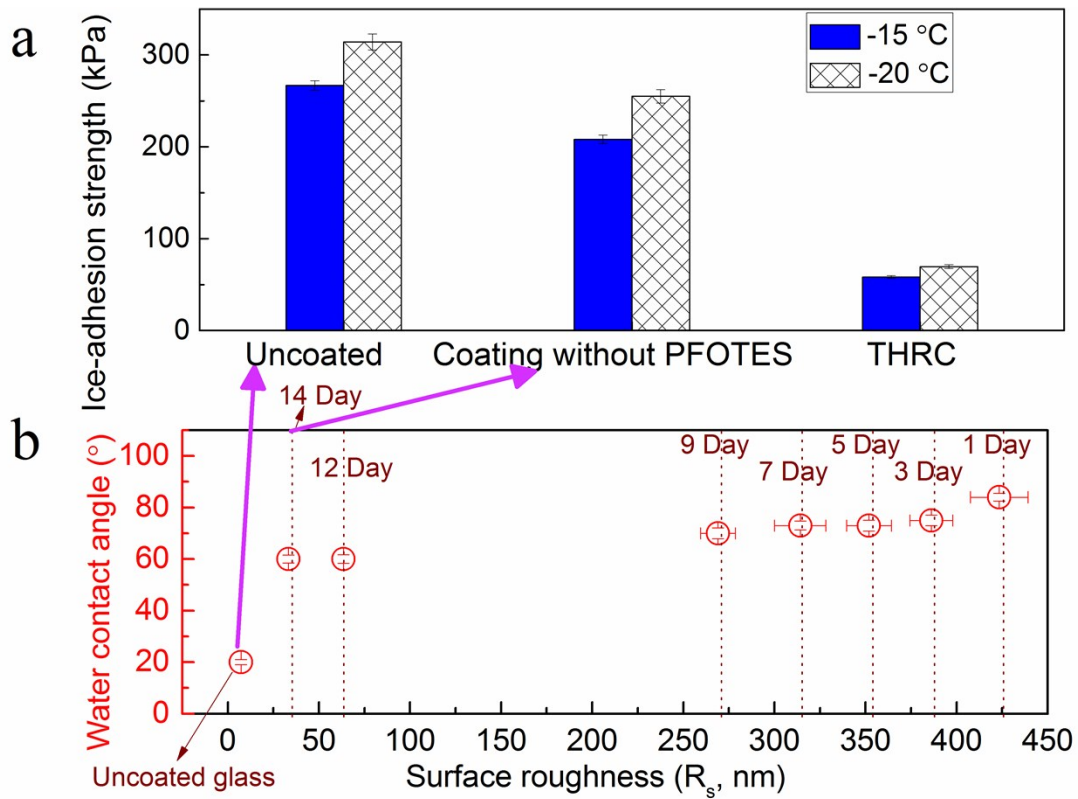
Fig. S7. (a) Ice-adhesion strength of uncoated glass, coating without PFOTES with 14 days' stirring and THRC coated glass. (b) Water contact angles of coatings without PFOTES at different stirring times versus surface roughness (root-mean-square roughness, R_S).
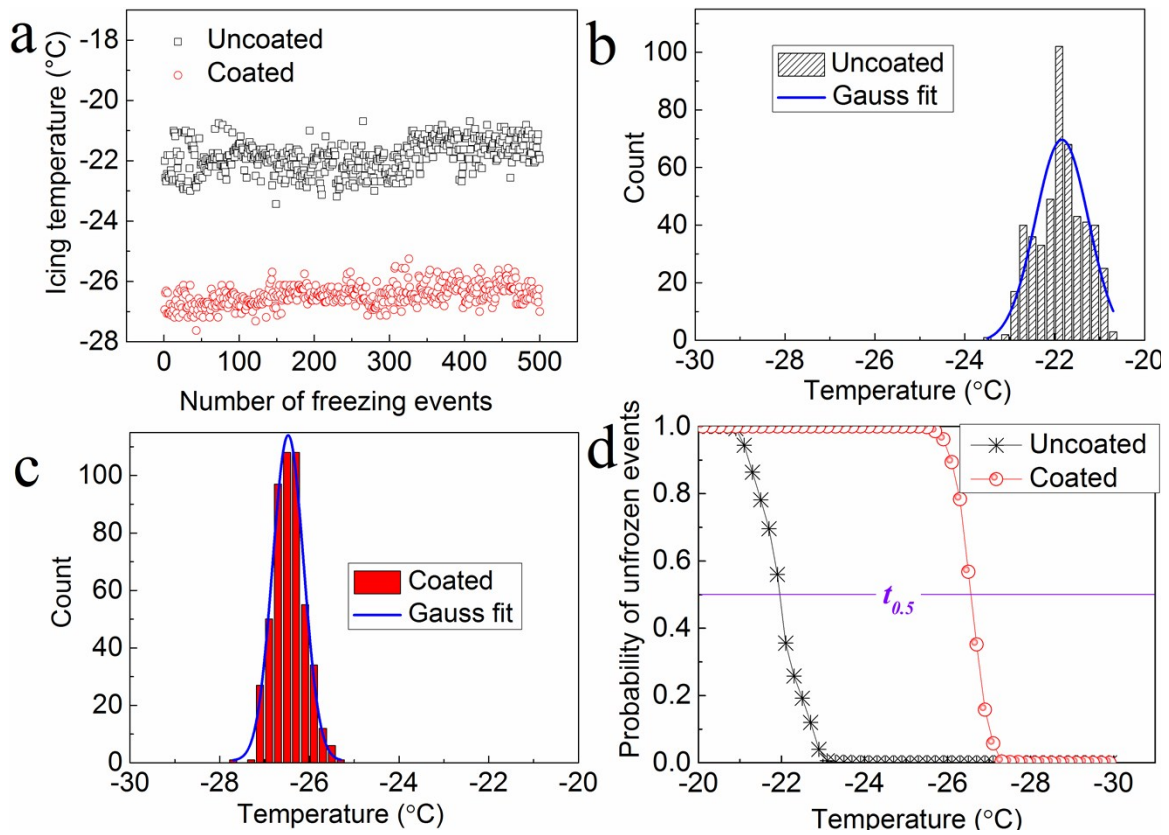
Fig. S8. (a) Ice-nucleation temperature of the THRC coated and uncoated glass, (b) histogram of the freezing events on uncoated glass and (c) THRC coated glass with bin width of 0.2 °C, (d) the survival curves of THRC coated and uncoated glass.

Table S2. Statistical values of the ice-nucleation temperature of THRC coated and uncoated glass.

	Uncoated	coated
Gauss peak value (°C)	-21.85	-26.47
$t_{0.5}$ (°C)	-21.96	-26.55

Table S3. Calculated radius and length of three-phase contact line between water droplet and solid surface.

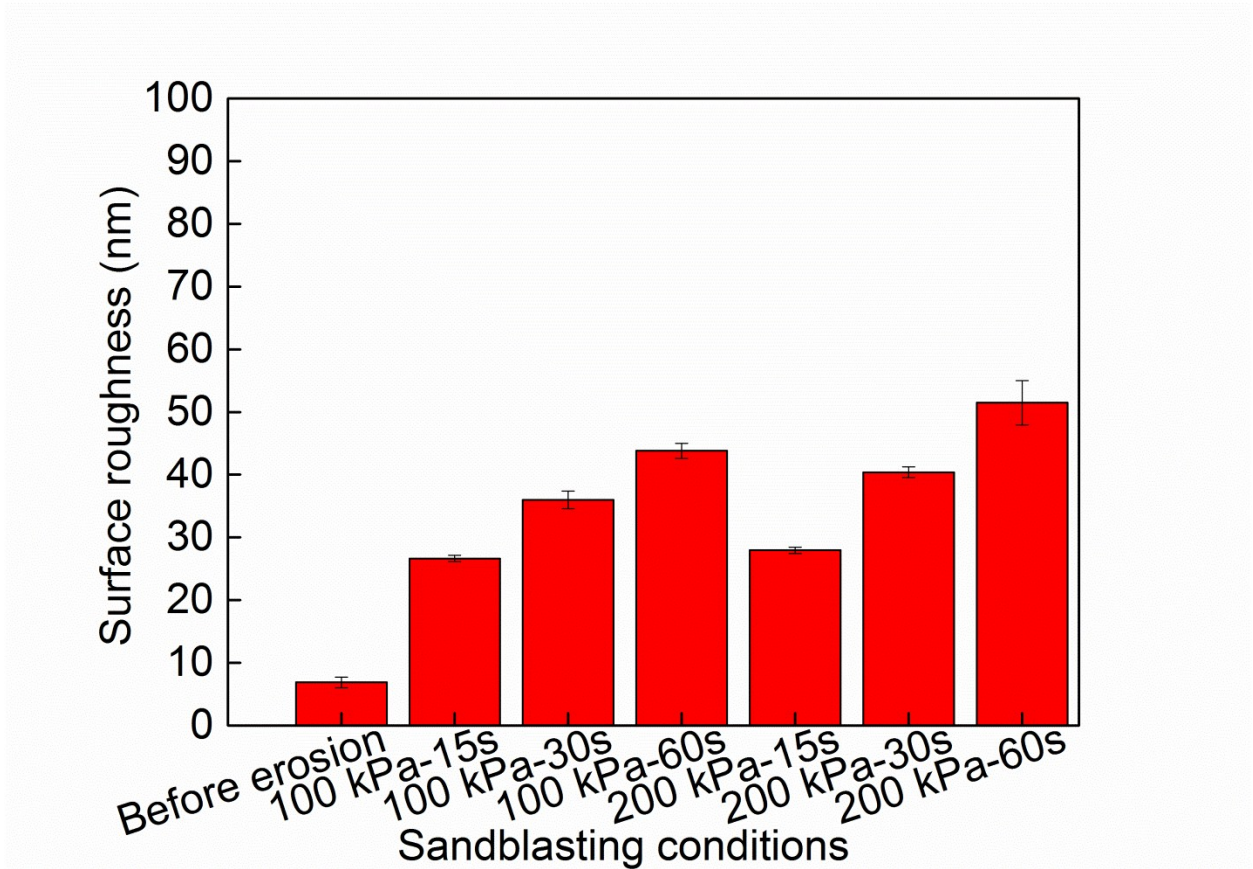|	θ	r (mm)	S (mm)
Uncoated	20	3.294	20.70
Coated	107	1.431	8.99

Fig. S9. The measured surface roughness of THRC coatings before and after sand erosion.

Video S1

This video shows the sliding behavior of different liquids (surface energy ranging from 72.8 to 22.1 mJ/m^2) on the THRC coated glass. (WMV format; 4.4 MB). The movie is played at 8-times accelerated speed.

Video S2

This video presents the icing delay results of 10μl water droplets on the THRC coated (top) and uncoated glass slides (bottom) as the temperature maintained at -15 °C. At the beginning, the droplet was bright and clear. Icing solidification on the water-solid contact area took place first. The droplet became blurry and dim. This stage happened in a few seconds. The time starts count only after the substrate surface temperature has reached the pre-set temperature of -15 °C. (WMV format; 4.2 MB). The movie is play at 16-times accelerated speed.

Video S3

This video was captured by a high-speed camera on the ice-nucleation process of a 10μl water droplet on the THRC coated and uncoated glass at -15 °C. (WMV format; 2.1 MB)

Video S4

This video presents the frost formation process of the THRC coated and uncoated glass slides as the temperature maintained at -15 °C. To shorten the video, the movie started at 7′30″ after the test begins and ended when frost formed on the edge of THRC coated glass. Comparison was made with an uncoated glass slide (left-hand side). (WMV format; 4.8 MB). The movie is play at 8-times accelerated speed.

1. J. S. Pérez, E. R. Porcel, J. C. López, J. F. Sevilla and Y. Chisti, *Chem. Eng. J.*, 2006, **124**, 1-5.

2. C. Collier, T. Vossmeyer and J. Heath, *Annu. Rev. Phys. Chem.*, 1998, **49**, 371-404.

3. J. N. Israelachvili, in *Intermolecular and surface forces*. (Academic press, ed. 3), United States, 2011, pp. 107-126 .

4. R. J. Plunkett, presented in part at American Chemical Society meeting, High Performance Polymers: Their Origin and Developmen , New York, US, 15-18 April, 1986.

5. D. Y. Mikhaylov and Y. H. Budnikova, *Russ. Chem. Rev.*, 2013, **82**, 835.

6. B. V. Velamakanni, J. C. Chang, F. F. Lange and D. S. Pearson, *Langmuir*, 1990, **6**, 1323-1325.

7. S. Amoriello, A. Bianco, L. Eusebio and P. Gronchi, *J. Sol-Gel Sci. Technol.*, 2011, **58**, 209-217.

8. K. Kamiya, T. Yoko, K. Tanaka and M. Takeuchi, *Journal of Non-Crystalline Solids*, 1990, **121**, 182-187.

9. M. Heise and G. Martin, *Macromolecules*, 1989, **22**, 99-104.

10. N. Poisson, G. Lachenal and H. Sautereau, *Vib. Spectrosc.,* 1996, **12**, 237-247.

11. S. Pazokifard, S. M. Mirabedini, M. Esfandeh and S. Farrokhpay, Chemeca 2011: Engineering a Better World: Sydney Hilton Hotel, NSW, Australia, September 2011:

12. U. Maitra, A. Gomathi and C. Rao, *J. Exp. Nanosci.*, 2008, **3**, 271-278.

13. P. Innocenzi, A. Martucci, M. Guglielmi, L. Armelao, S. Pelli, G. Righini and G. Battaglin, *J. Non-Cryst. Solids*, 1999, **259**, 182-190.

14. E. Lataste, A. Demourgues, H. Leclerc, J. M. Goupil, A. Vimont, E. Durand, C. Labrugère, H. Benalla and A. Tressaud, *J. Phys. Chem. C*, 2008, **112**, 10943-10951.

15. Q. T. Fu, E. J. Liu, P. Wilson and Z. Chen, *Phys. Chem. Chem. Phys.*, 2015, **17**, 21492-21500.

16. P. Wilson, A. Heneghan and A. Haymet, *Cryobiology*, 2003, **46**, 88-98.

17. P. Wilson and A. Haymet, *Phys. Chem. Chem. Phys.*, 2009, **11**, 2679-2682.

18. P. W. Wilson, K. E. Osterday, A. F. Heneghan and A. D. Haymet, *J. Biol. Chem.*, 2010, **285**, 34741-34745.

19. T. Verho, C. Bower, P. Andrew, S. Franssila, O. Ikkala and R. H. A. Ras, *Adv. Mater.*, 2011, **23**, 673-678.

20. P. W. Wilson, W. Lu, H. Xu, P. Kim, M. J. Kreder, J. Alvarenga and J. Aizenberg, *Phys. Chem. Chem. Phys.*, 2013, **15**, 581-585.

21. P. Hao, C. Lv and X. Zhang, *Appl. Phys. Lett.*, 2014, **104**.